1 *Article*

2,3 Plasmonic refractive index sensor with high figure of merit based on concentric-rings resonator

4,5 **Zhaojian Zhang [1], Junbo Yang [2], *, Xin He, Jingjing Zhang, Jie Huang, Dingbo Chen and Yunxin Han**

6,7 [1] College of Liberal Arts and Sciences, National University of Defense Technology, Changsha 410073, China; 376824388@qq.com

8,9 [2] Center of Material Science, National University of Defense Technology, Changsha 410073, China; yangjunbo008@sohu.com

10 * Correspondence: yangjunbo008@sohu.com

11 **Abstract:** A plasmonic refractive index (RI) sensor based on metal-insulator-metal (MIM)
12 waveguide coupled with concentric double rings resonator (CDRR) is proposed and investigated
13 numerically. Utilizing the novel supermodes of the CDRR, the FWHM of the resonant wavelength
14 can be modulated, and a sensitivity of 1060 nm/RIU with high figure of merit (FOM) 203.8 is realized
15 in the near-infrared region. The unordinary modes as well as the influence of structure parameters
16 on the sensing performance are also discussed. Such plasmonic sensor with simple framework and
17 high optical resolution could be applied to on-chip sensing systems and integrated optical circuits.
18 Besides, the special cases of bio- sensing and triple rings are also discussed.

19

20 **Keywords:** plasmonic sensor; high figure of merit; concentric double rings resonator
21

22 **1. Introduction**

23   Surface plasmon polaritons (SPPs) are electromagnetic fields propagating along the interface of
24 metal-insulator, and have been widely discussed for several decades due to the ability to modulate
25 light in nanoscale as well as break the diffraction limit [1]. Recently, many kinds of plasmonic devices
26 have been investigated such as filters [2], absorbers [3], splitters [4] and sensors [5]. Among these,
27 plasmonic sensors have drawn more attention, because compared with traditional optical sensors
28 such as fiber sensors and silicon-based sensors, plasmonic sensors have much smaller size with
29 comparable sensing performance, which means they are more suitable for integrating [6]. Various of
30 plasmonic sensors have come out lately such as refractive index sensors [7], temperature sensors [8],
31 phase sensors [9] and gas sensors [10].
32   The metal-insulator-metal (MIM) waveguide is one of the basic plasmonic waveguides with the
33 capability to confine light within considerable propagating length [11], and many works of sensor are
34 based on this structure [12-20]. As a sensor, it requires both high sensitivity (S) and high figure of
35 merit (FOM) to promise an excellent performance with high optical resolution. Great efforts have
36 been made to improve sensitivity on MIM plasmonic sensors, but longer wavelength always suffers
37 from wider FWHM [12-15], which means lower FOM. Recently, Fano resonance has been universally
38 applied to enhance FOM which results from structure symmetry break or dark-bright resonance
39 interference, and it has an asymmetric spectral line shape with narrower FWHM [16-20]. But such
40 resonance is unstable and can be easily broken due to phase or mode mismatch which could be
41 caused by localized corrosion of structure, change of localized refractive index and so on.
42   In this study, a traditional MIM plasmonic sensor coupled with simple concentric double rings
43 resonator (CDRR) is proposed. Utilizing the special supermodes, the FOM of that can be significantly
44 improved to as high as 272.3 in the visible-light region without Fano resonance, as well as 203.8 in
45 the near-infrared region. Such value of FOM is quite larger than other recent works [5, 7, 12-18]. The
46 peculiar properties of CDRR supermodes and the impact of structure parameters on sensing

47 performance are also discussed. The 2D Finite-Difference Time-Domain (FDTD) solution is used to
48 simulate this structure with perfectly matched layer (PML) boundary condition.

49 **2. Structural Model and Theory Analysis**

50   As shown in Fig. 1, a MIM waveguide coupled with a CDRR is proposed. The silicon substrate
51 is plated with silver, which is chosen for the relative low loss [24]. The waveguides are etched on the
52 silver surface. Such structure can be fabricated by the method of focused ion beam (FIB) [34]. As
53 shown in 2D picture, the grey and white areas represent silver and air, respectively. The permittivity
54 of air is set as $\varepsilon_i = 1$, as for silver (Ag) the Drude model is utilized as follows [2]:

$$\varepsilon_m = \varepsilon_\infty - \frac{\omega_p^2}{\omega(\omega + i\gamma)} \tag{1}$$

56   Here ε_∞ gives the medium constant for the infinite frequency, ω_p refers to bulk frequency for
57 plasma, γ means damping frequency for electron oscillation, and ω shows incident light angular
58 frequency. The parameters for silver are $\varepsilon_\infty = 1$, $\omega_p = 1.37 \times 10^{16}$ Hz, and $\gamma = 3.21 \times 10^{13}$ Hz.
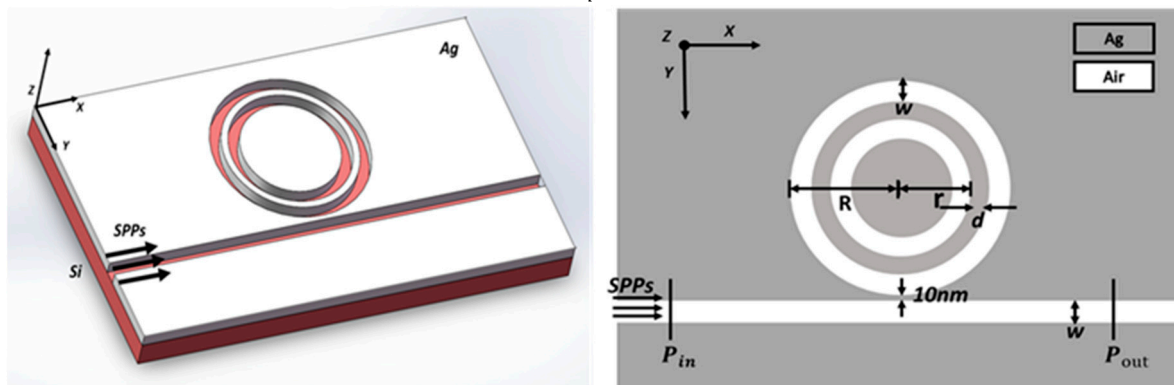
60   **Figue.1** The 3D and 2D picture of the plasmonic sensor.

61   In this structure, $R = 350$nm and $r = 270$nm is the radius of the outer and inner ring,
62 respectively. The width of the waveguide is set as $w = 50$nm, and the gap between inner and outer
63 ring is $d = 30$nm. The gap between CDRR and bus waveguide is $g = 10$nm. To collect the incident
64 and transmitted power, two monitors are put respectively at P_{in} and P_{out}. The transmittance of
65 power can be calculated by $T = P_{out}/P_{in}$.
66   TM mode SPPs can propagate at the surface of interface in the waveguide when coupled into
67 the MIM structure. Compared with incident wavelength the width of the bus waveguide is much
68 smaller, so fundamental TM mode can exist only. The dispersion relation of this fundamental mode
69 is described as follows [11]:

$$\frac{\varepsilon_i p}{\varepsilon_m k} = \frac{1 - e^{kw}}{1 + e^{kw}} \tag{2}$$

$$k = k_0 \sqrt{(\frac{\beta_{spp}}{k_0})^2 - \varepsilon_i}, \, p = k_0 \sqrt{(\frac{\beta_{spp}}{k_0})^2 - \varepsilon_m} \tag{3}$$

$$\beta_{spp} = n_{eff} k_0 = n_{eff} \frac{2\pi}{\lambda} \tag{4}$$

73   Here w refer to the width of bus waveguide, λ shows incident light wavelength in vacuum, ε_i
74 and ε_m give the relative dielectric and metal permittivity, β_{spp} and n_{eff} are propagation constant
75 and effective refractive index of SPPs, and $k_0 = 2\pi/\lambda$ means wave number.

76
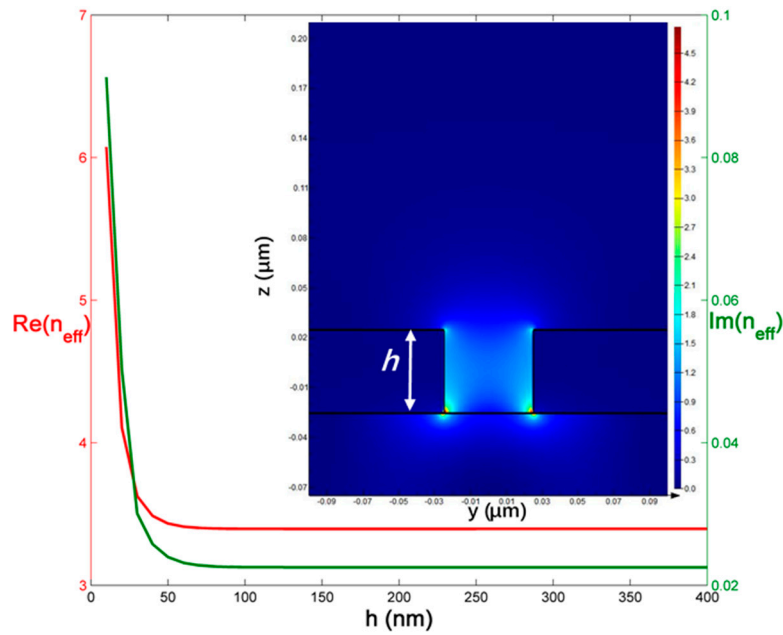
77   **Figure. 2** The relationship between the effective refractive index of the SPPs and the height of the
78   waveguide at wavelength 850 nm. The inset is the distribution $|P_x|$ of the fundamental mode at 850
79   nm when h=50 nm.

80   Most of the proposed and designed MIM plasmonic devices have used 2D simulation, which is
81   infinite in one dimension, to test the performance of the devices with much shorter simulation time
82   and lower loss [26], and so is this work. But the height of the waveguide has significant effect on the
83   loss of the system, which has to be considered for practical processing. Here, the relationship between
84   the effective refractive index of the SPPs and the height of the waveguide at 850 nm is shown in Fig.
85   2. As the height increases, both real and imaginary part of the n_{eff} will decrease at start, which is
86   due to the decrease of the fraction corresponding to the modal power in the metal at interfaces. The
87   reduce of the imaginary part of n_{eff} means less loss, which can lead to longer propagation length
88   [25]. However, when greater than a certain height, n_{eff} will remain stable. If continuing improving
89   the height, n_{eff} will approach the value in 2D simulation, which is the $h \rightarrow \infty$ case. The distribution
90   $|P_x|$ of the fundamental mode at 850 nm when h=50 nm is presented in the inset of Fig. 2. At other
91   wavelengths, the outcome will be similar. After comparing the values at different wavelengths, the
92   most suitable height can be selected. Our result is agreed with [25].

93
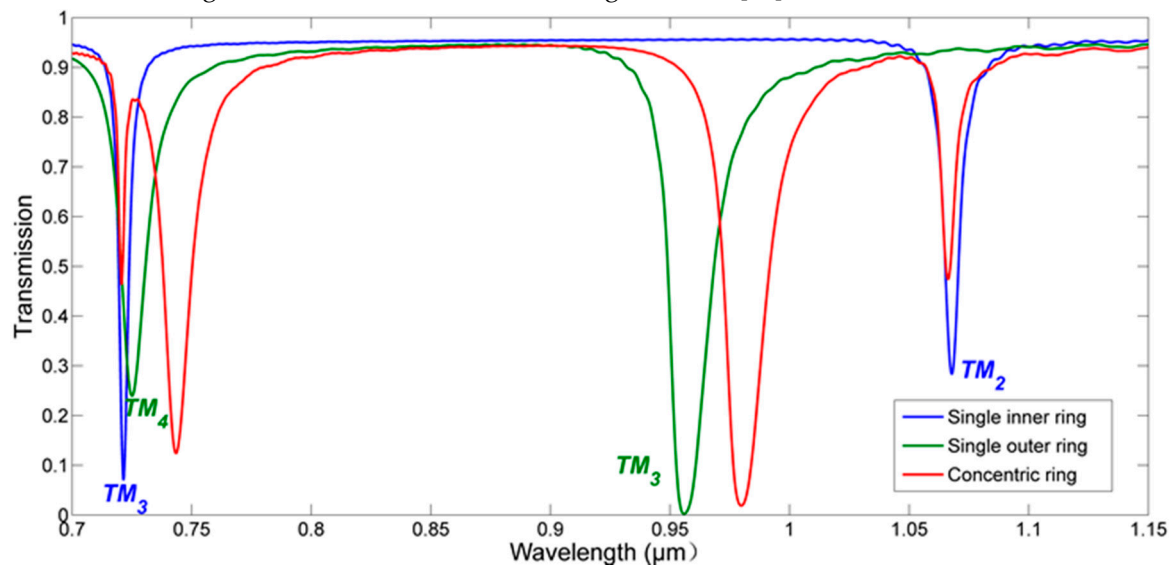
94 **Figure. 3** The transmission spectra of MIM waveguide coupled with single inner (outer) ring or
95 CDRR.

96 The transmission spectra of MIM waveguide coupled with single inner (outer) ring or CDRR are
97 shown in Fig. 3. In order to illuminate the principle of CDRR better, the gap between bus waveguide
98 and single inner (outer) ring is set as 30nm (10nm). Fig. 3 indicates that the transmission spectrum of
99 CDRR is almost the superposition of the other two spectra with slight shifts, and the FWHM of the
100 mode near 1060nm becomes narrower. For a single ring resonator, the resonance condition can be
101 described as [5]:

102
$$N\lambda = \mathrm{Re}(n_{eff})L_{eff}, N = 1, 2, 3... \tag{5}$$

103 Where n_{eff} refers to the effective refractive index of the ring resonator which can be solved by
104 Eq. (2–4), L_{eff} means effective perimeter, generally refers to the average of the inner and outer
105 perimeters. N refers to mode number which is an integer.

106 For the CDRR, the resonance condition is the superposition of that for single ring, and the shift
107 of resonant wavelength comes from the change of effective index of each ring resulting from the
108 interaction between each other.
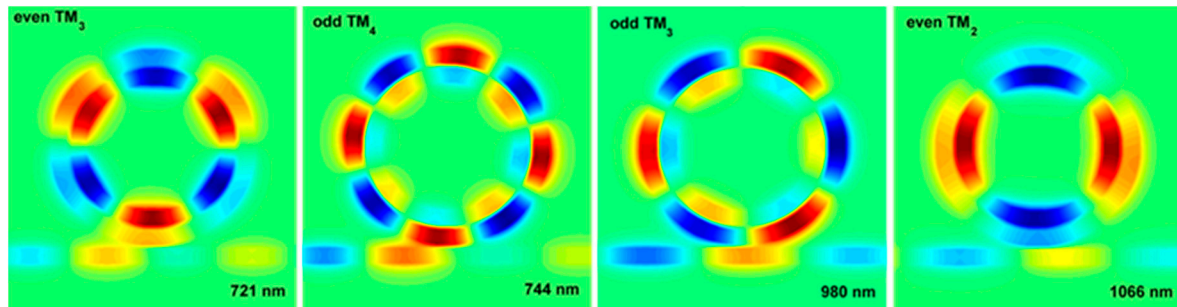
109
110 **Figure. 4** The supermodes of CDRR.

111 It is found that the modes of CDRR exist in the form of supermodes, which means the inner and
112 outer ring have resonance simultaneously. And the novel supermodes of CDRR are introduced as
113 shown in Fig. 4. However, we notice that there are only two kinds of supermodes: when the energy
114 is mainly trapped in outer ring, the mode in the inner ring will have anti phase; when mainly trapped
115 in inner ring, it is in phase. Refer to the supermodes between two parallel waveguides [21], the two
116 supermodes could be called odd mode (with anti-phase) and even mode (with in-phase). The
117 mechanism of such supermodes can be explained by the coupled-mode theory (CMT) [22]. The
118 propagation constant in the ring resonator can be derived with Eq. (5):

119
$$\mathrm{Re}(\beta) = \frac{2\pi\,\mathrm{Re}(n_{eff})}{\lambda} = \frac{2\pi}{\lambda} \cdot \frac{N\lambda}{2\pi R_{eff}} = \frac{N}{R_{eff}} \tag{6}$$

120 Where R_{eff} is the effective radius of the ring resonator, and the propagation constant of odd
121 (even) mode in the system of two parallel single-mode waveguides is as follows [22]:

122
$$\beta_{odd} = \overline{\beta} - \Delta\beta \tag{7}$$

123
$$\beta_{even} = \overline{\beta} + \Delta\beta \tag{8}$$

124
$$\overline{\beta} = \frac{\beta_1 + \beta_2}{2}, \quad \Delta\beta = \frac{1}{2}\sqrt{4K^2 + (\beta_1 - \beta_2)^2} \tag{9}$$

125 Here, $\overline{\beta}$ represents the average propagation constant, β_1 (β_2) is the propagation constant for a
126 single waveguide without coupling, and K is the coupling coefficient. In the condition of the
127 codirectional coupling, K is a pure imaginary number [22]. Eq. (7-8) shows that the $\mathrm{Re}(\beta_{even})$ is
128 always larger than $\mathrm{Re}(\beta_{odd})$. Since the CDRR could be considered as two parallel bend waveguides
129 with periodicity, this mode expression can also be applied. Now the CDRR system is considered as a
130 kind of single-ring resonator, the effective radius of which is determined by the energy distribution.
131 When the energy is mainly trapped in the outer side, the effective radius is larger leading to smaller

132   propagation constant according to Eq. (6), bringing about the odd mode with anti-phase in the CDRR.
133   Otherwise, it will be an even mode with in-phase.

134
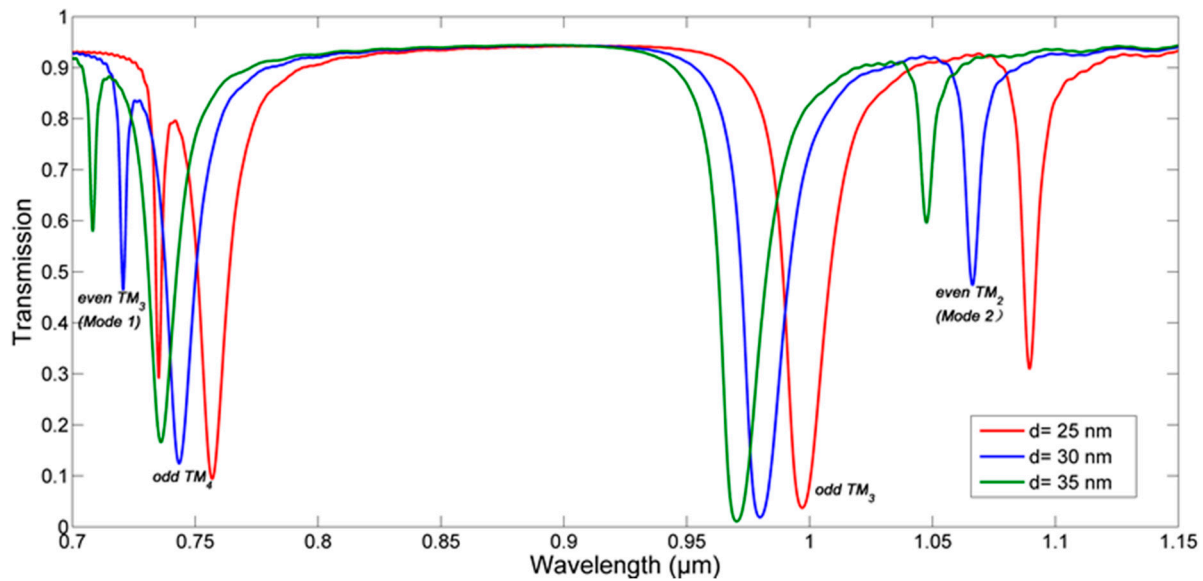
135   **Figure. 5** The transmission spectra correspond to different gaps.

136   By changing the radius of inner ring (which also means the change of the gap d), the transmission
137   spectra correspond to different gaps is obtained in Fig. 5. Obviously, the resonant wavelength will
138   have a blue shift when increasing the gap. The Fig. 6(b) shows the details, and we find that for even
139   modes, the resonant wavelength has a linear relationship with gap; for odd modes, it is nonlinear. It
140   can be explained by the effective index. When changing the radius of inner ring linearly, the effective
141   index of outer ring will be influenced and have a nonlinear change, leading a nonlinear relationship
142   between odd-mode (which can be regarded as mode of inner ring approximately according to the
143   energy distribution) resonant wavelength and gap. However, the inner ring will suffer both radius
144   and gap change, and that will keep its effective index unchanged, bringing about the linear
145   relationship between even-mode resonant wavelength and the radius of inner ring as Eq. (5). Such
146   conclusion can be useful for designing the CDRR.

147
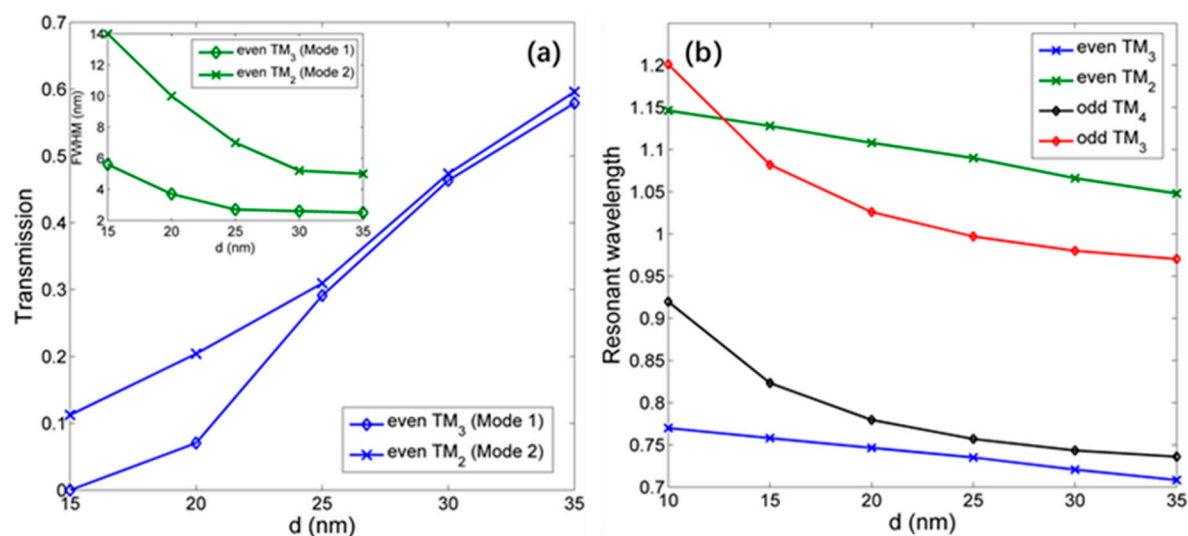
148   **Figure. 6** (a)The relationship between Transmission (FWHM) and gap. (b) The relationship between
149   resonant wavelength and gap.

150   Apparently, the even mode has much narrower FWHM, therefore the two even modes (even
151   TM_3 and TM_2) are investigated next which is assumed as mode 1 and mode 2, respectively. Fig.6 (a)
152   shows the relationship between gap d and FWHM (transmission). When increasing the gap, the
153   FWHM of even mode will be narrower, meanwhile suffering from the increase of transmission. It is
154   due to the special mode distribution of even mode, the energy of which is mainly trapped in the inner
155   ring, and the outer ring suppresses the energy loss which is beneficial for energy storage. As the inner
156   and outer rings have the same symmetry, the supermode is stable and has the single-ring mode
157   features. Such even modes are potential to generate ultra-high Q factors, which is defined as Q =
158   $\lambda/FWHM$. With gap 30nm, the Q for mode 1 can reach 277 and for mode 2 is 205. The Q will be larger
159   with increasing gap, however there is a trade-off between Q and transmission.

160   **3. Refractive Index Sensing**

161   Considering the balance between FWHM and transmission, the gap d is chosen to be 30nm. The
162   plasmonic sensor filled with media is shown in Fig. 7, and Fig. 8 presents the transmission spectra
163   with different filling dielectric in the CDRR. The refractive index of dielectric is increased from 1 to
164   1.1 with the step 0.025, leading to a red shift of the spectra. The sensing capabilities is defined as
165   follows [23]:

166
$$S = \frac{\triangle\lambda}{\triangle n}, FOM = \frac{S}{FWHM} \tag{10}$$

167
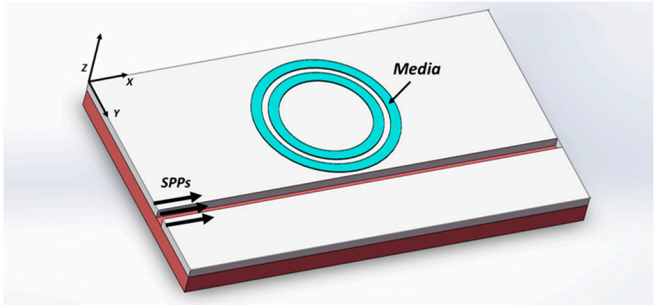
168   **Figure. 7** The 3D picture of the plasmonic sensor filled will media.

169   The sensitivity S is described as the resonant wavelength shift when the dielectric has a unit
170   change. Since the optical resolution is also crucial for sensors, a high figure of merit (FOM) is needed.
171   By fitting the line in the inset of Fig. 8, the sensitivity 708nm/RIU of mode1 and 1060nm/RIU of mode
172   2 are obtained. The FWHM of each is 2.6nm and 5.2 nm, leading to the high FOM which is 272.3 and
173   203.8, respectively. It must be mentioned that such value of FOM is quite larger than other recent
174   works as shown in Table. 1. Although some works achieved a higher figure up to hundreds of
175   thousands [19,20], the FOM definition of these works is different, which always refers to FOM^*[23].

176   **Table. 1** Comparison of S and FOM reported in various Plasmonic sensor.

Reference	S (nm/RIU)	FOM
Chen, L., et al. [5]	1496	124.6
Yan, Shu Bin, et al. [13]	868.4	43.9
Tang, Y., et al. [16]	1125	74
Zhang, Zhidong, et al. [17]	596	7.5

Zafar, Rukhsar, and M. Salim. [18]	1060	176.7
This paper	1060	203.8

Due to the higher sensitivity with excellent FOM in the near-infrared region, mode 2 is further studied then. The radius of CDRR is increased with the gap d fixed at 30nm, and the spectra are given in Fig. 9(a). When the outer radius raises from 350nm to 400nm with the interval 10nm, the sensitivity is 1112 nm/RIU, 1152 nm/RIU, 1196 nm/RIU, 1224 nm/RIU and 1280nm/RIU respectively from Fig. 9(b), and FOM is 185.3, 164, 149.5, 153 and 150.4 respectively. Obviously, increasing the size of CDRR can improve the sensitivity performance of the sensor with the cost of lower FOM, which may respectively arise from the longer optical path and higher dissipation of energy.
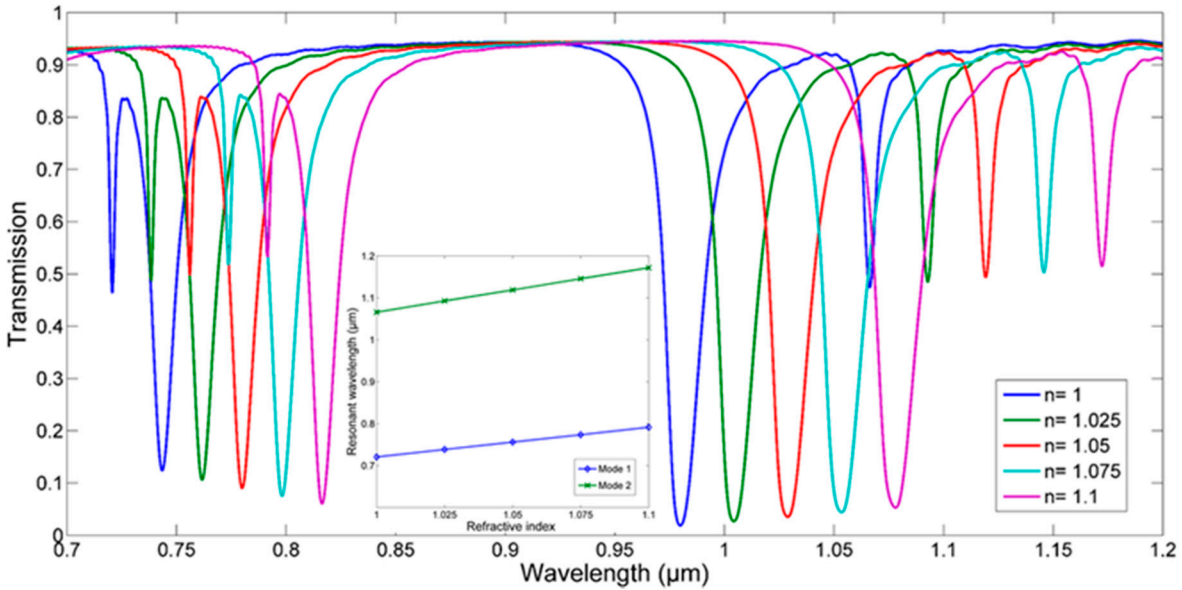
Figure. 8 The transmission spectra with different filling dielectric in the CDRR. The inset shows the relationship between refractive index and resonant wavelength.
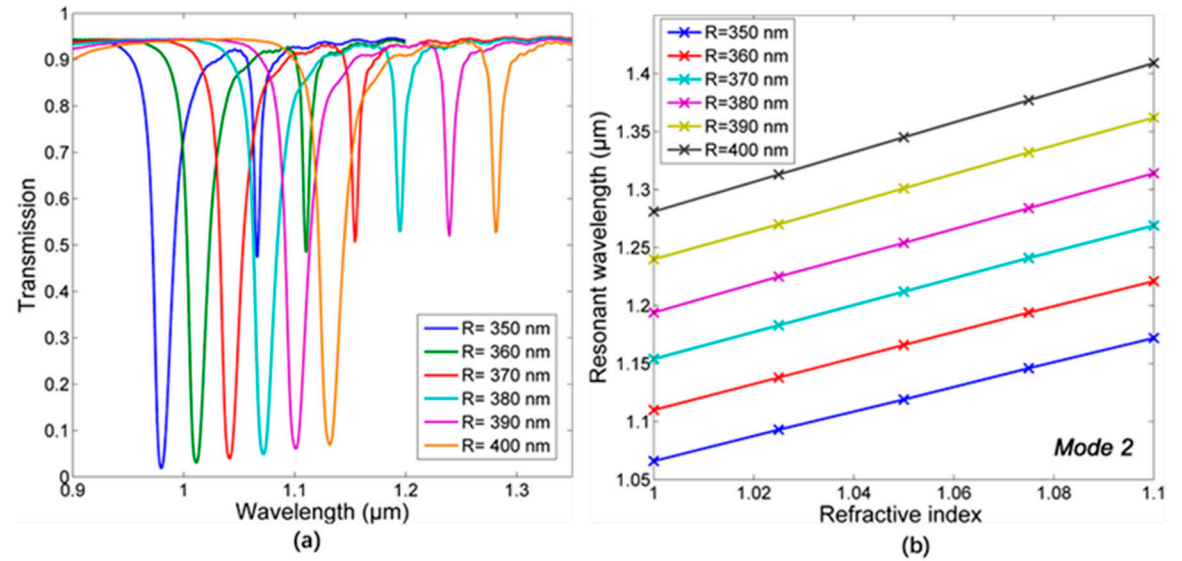
Figure. 9 (a) the spectra with different radius of CDRR. (b) the ling fitting between refractive index and resonant wavelength.

Comparing with Fano resonance, which is the hotspot for sensing recently [27], this structure has a superiority on stability. Although Fano resonance has a narrow FWHM leading to high FOM,

192 few works pay attention to the instability of this state. Fano resonance occurs when a discrete state
193 interferes with a continuum band of states, the shape of the special transmission spectrum can be
194 described by Fano formula [27]:

$$Y = \frac{(q+X)^2}{1+X^2} \qquad (11)$$

195

196 Where $q = cot\delta$ is the Fano parameter, δ is the phase shift of the continuum between two
197 modes, depending on geometric and material parameters of the system [27], which can be caused by
198 corrosion, fabrication errors, change of localized refractive index and so on. Fig. 10 presents the
199 spectrum shape corresponding to different q values. Due to the character of cot function, little phase
200 shift will cause significant change of q, leading to the breaking of the high-q Fano shape, then bring
201 about the decline of sensing performance.

202
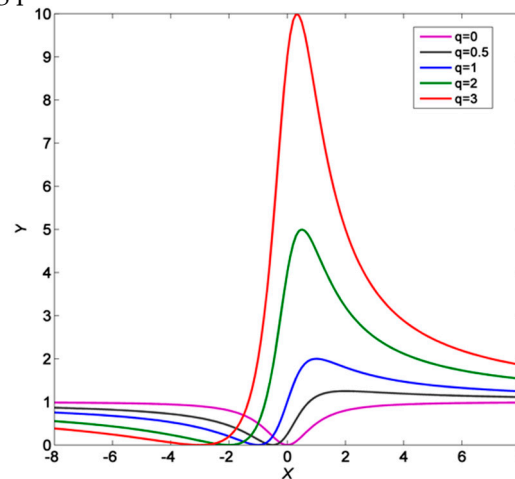
203 **Figure. 10** The Fano spectrum shape corresponding to different q values.

204 The supermode in CDRR is based on traditional micro-ring resonance, which is not that fragile.
205 To test the stability of this sensor, a 5×5 nm square defect is inserted at two different positions of
206 CDRR respectively as given in Fig. 11 (b) and (c). From the corresponding transmission spectrum of
207 mode 2 shown in Fig. 11(a), the defect on outer (inner) ring only has influence on the resonance of
208 outer (inner) ring, which can make resonant wavelength shift or create new mode. However, the
209 mode 2 still exists with narrow FWHM in both cases, only suffers from little lower absorption or
210 resonant wavelength change. The corresponding distributions $|H_z|$ of mode 2 with defect are
211 presented in Fig. (d) and (e).

212
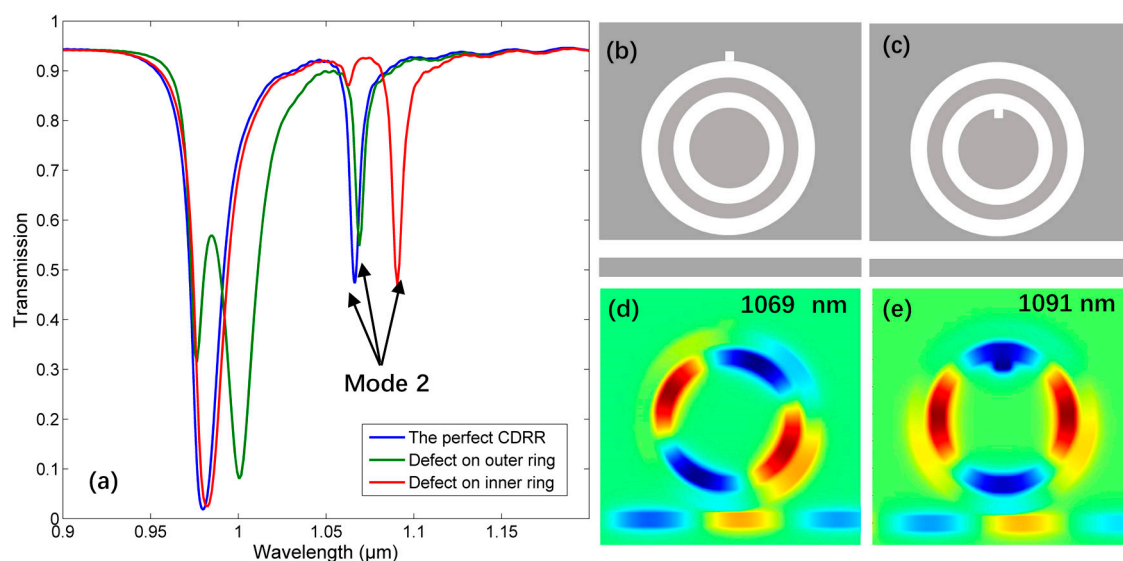
213   **Figure. 11** (a) The transmission spectrum of mode 2 with defect. (b) CDRR with defect on outer ring.
214   (c) CDRR with defect on inner ring. (d) The $|H_z|$ of mode 2 with defect on outer ring. (e) The $|H_z|$ of
215   mode 2 with defect on inner ring.

4. Bio-sensing

217   Here, the application for bio-sensing is discussed, the same structure parameters are chosen with
218   outer ring radius 350nm and gap 30 nm, and still only mode 2 is focused. Since water is one of the
219   most common solvents used in chemical and biological applications, it is necessary to test the
220   performance of the sensor in water (n=1.33) as presented in Fig. 12 (a). Considering the concentration
221   of solution can be reflected by the refractive index (RI), a set of different RI values around the water
222   are used to measure the sensitivity and FOM, the transmission spectrum is given in Fig. 12 (b).
223   According to Fig. 12 (c), the sensitivity in the water is 1061 nm/RIU, and the FOM of 193 can be
224   achieved, which can prove this sensor still has excellent performance in water.
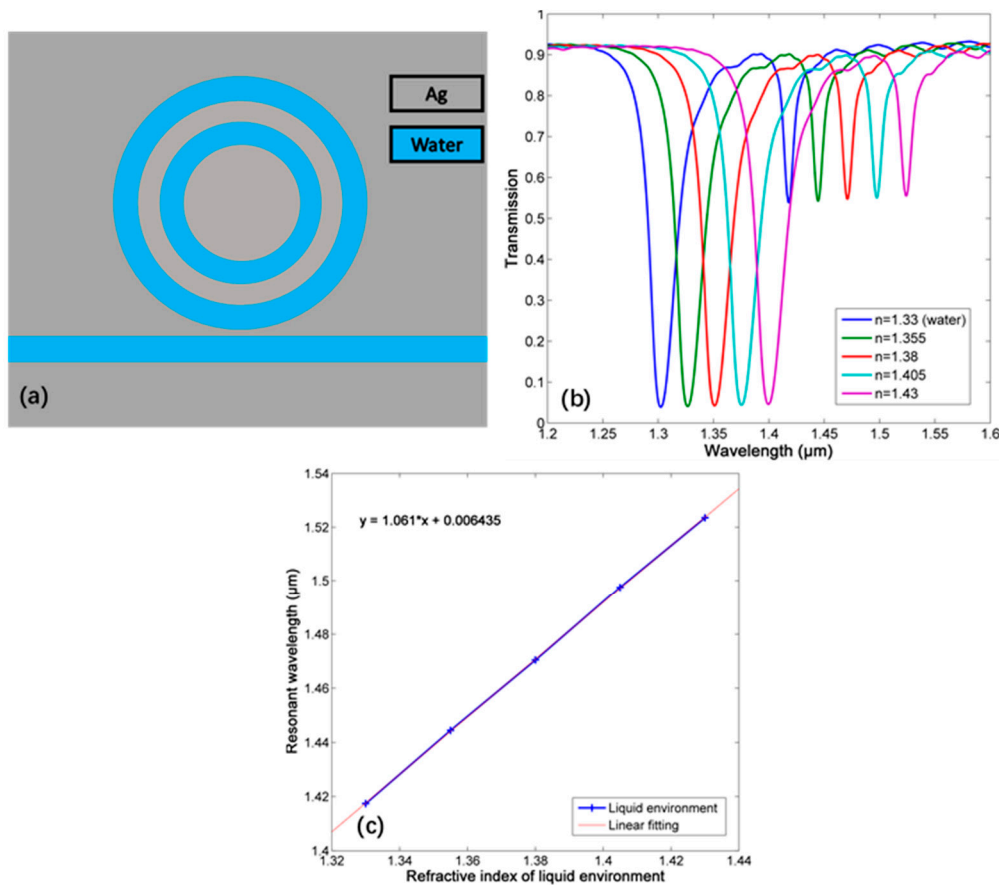
226   **Figure. 12** (a) Sensor at water. (b) The transmission spectrum of sensor in liquid environment. (c) The
227   relationship between refractive index and resonant wavelength of mode 2.

228
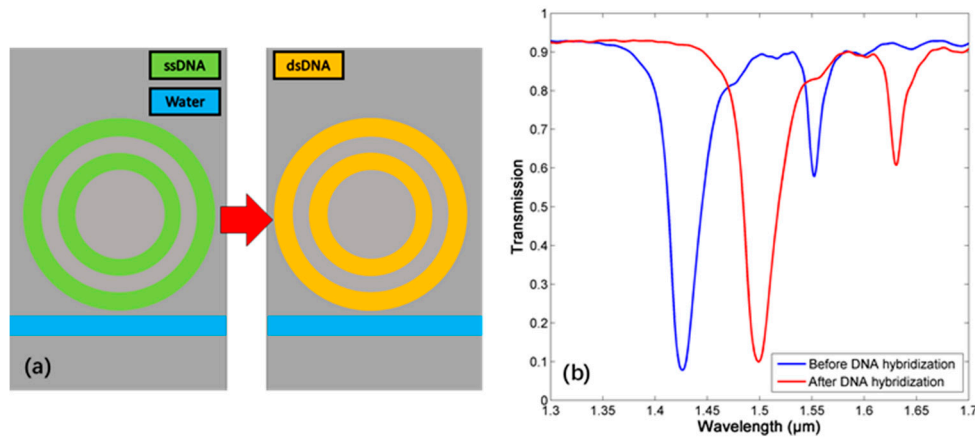
Figure. 13 (a) The process of DNA hybridization. (b) The transmission spectrum before and after DNA hybridization.

229
230

Therefore, such structure can be a sensitive label-free and compact biosensor. A special case for the detection of the DNA hybridization is shown as follows. After the DNA hybridization, i.e., when single strand DNA (ssDNA) becomes double strands DNA (dsDNA), the RI of DNA layers will change from 1.456 to 1.53 [28]. If a layer of ssDNA is implanted inside the resonator, the DNA hybridization can be detected as shown in Fig. 13. After the hybridization, the resonant wavelength of mode 2 shift from 1553 nm to 1631 nm with high optical resolution, which can be probed easily.

237
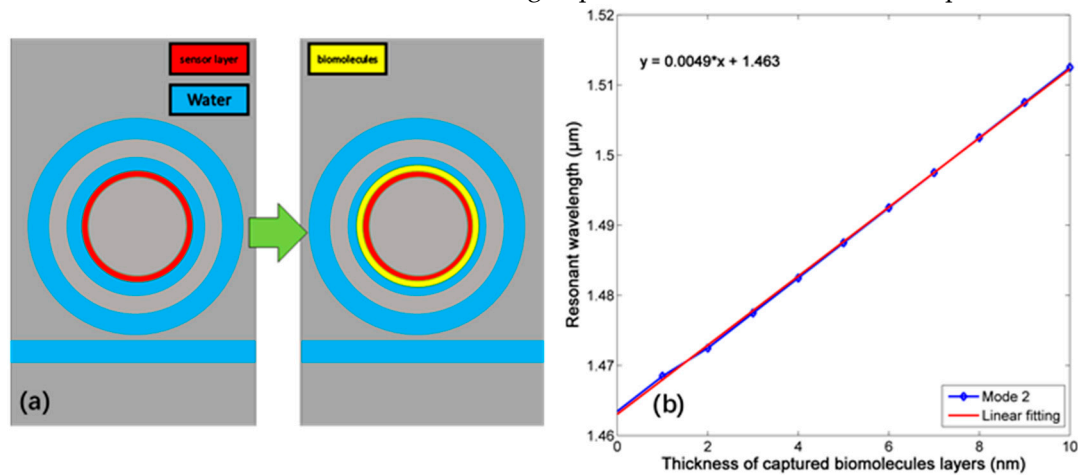
Figure. 14 (a) The selective biochemical process. (b) The relationship between resonant wavelength and thickness of captured layer.

238
239

Another bio-application of this sensor is to detect the biomolecules attached to the inner wall of the resonator. We assume that a combined sensor layer of thickness t_{cap}, which consists of an activating intermediate layer and a capture layer, has been immobilized onto the wall of inner ring, which can capture a layer of biomolecules of thickness t_{bio} through a selective biochemical process such as antigen-antibody binding process [29-31] as shown in Fig. 14 (a). The RI and material dispersion of the biolayers will depend on how the biomolecules are oriented. Here we neglect the dispersion of the biolayers and assume that they have the same RI of 1.45, close to that of silica [30], which is a realistic assumption proved by experimental measurements with MOF biosensors [32]. Assuming $t_{cap} = 10nm$, the relationship between resonant wavelength and thickness of captured layer t_{bio} is shown in Fig. 14 (b), and a thickness sensitivity ($S' = \Delta\lambda/\Delta t$) of 4.9 nm/nm can be gained. Comparing with traditional micro-structured optical fiber (MOF) biosensors [32], this plasmonic biosensor has comparable sensitivity, higher optical resolution and much smaller footprint. It has to be mentioned that from Fig. 12 (b) and Fig. 13 (b), the FWHM of mode 2 can remain narrow within a

253 wide environment effective RI range. Since layers effect can be equal to the change of effect RI
254 essentially [33], the detection for the layer can still possess the character of high optical resolution.
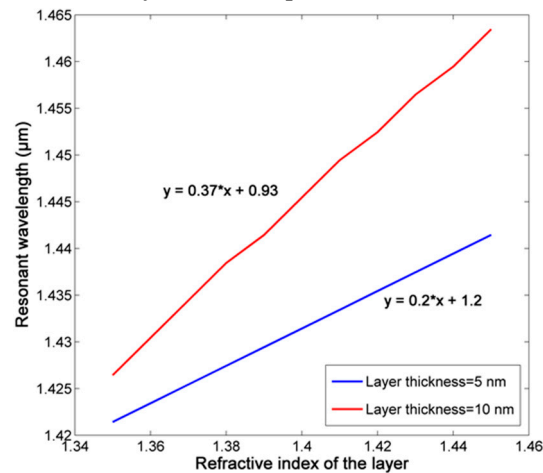
256 **Figure. 15** The relationship between layer RI with certain thickness and resonant wavelength.

257 Finally, considering a biomolecules layer attached to the wall of inner ring with a certain
258 thickness t, the sensitivity for the layer RI is measured for the case t= 5 nm and t= 10 nm, shown as
259 Fig. 15. We choose both sizes because these are the most common feature scale of single biomolecule
260 [31], and the sensitivity 200 nm/RIU (t= 5 nm) and 370 nm/RIU (t= 10 nm) can be realized with high
261 optical resolution.

262 **5. Case of Triple Ring**

263 Out of interest, the case of concentric triple rings resonator (CTRR) is proposed with w= 50 nm,
264 d=15 nm, g=10 nm and R= 350 nm. The transmission spectrum and mode distribution are presented
265 in Fig. 16. Here, assuming that the binary *0/1* represent a set of opposite phases, and the array *[1 b c]*
266 describes the supermode (we set outer-ring-phase as 1), where b, c give the phase of mode in middle
267 ring and inner ring. After checking the supermodes for a wide wavelength range, we found that only
268 three kinds supermodes exist: *[1 1 0]*, *[1 1 1]* and *[1 0 1]*.
269 For supermode *[1 1 1]*, an ultra-narrow FWHM can be reached, as shown in Fig. 16 when λ =
270 591 nm and 864 nm. When λ = 591 nm, the FWHM is nearly 1 nm, and an ultra-high Q= 591 can be
271 gained. The reason is that in this supermode, most energy is trapped in the inner ring. Therefore, the
272 outer double rings can suppress the energy loss. However, this supermode may suffer from the low
273 energy absorption, such as that at 864 nm. Additionally, CTRR will possess a great many resonant
274 wavelengths, it may bring about some disturbances on sensing. This structure may have potential
275 applications to be found.
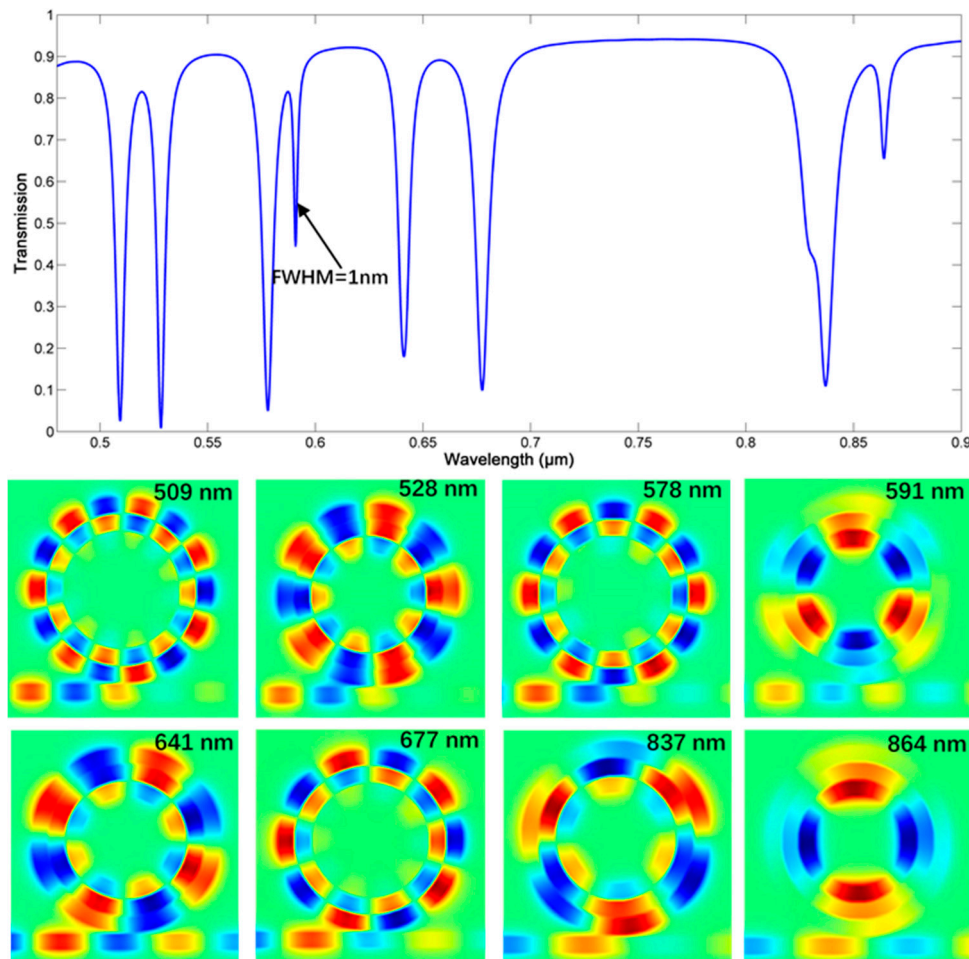
Figure. 16 The transmission spectrum and mode distribution of CTRR.

6. Conclusions

In summary, a sensor based on MIM waveguide coupled with a CDRR is investigated in the near-infrared region, and a high sensitivity with ultra-high FOM is obtained in RI-sensing and bio-sensing. The special features of supermodes in CDRR is discussed, presenting that the even mode can produce ultra-narrow FWHM. The special case of triple rings is also discussed. In addition, such structure also provides the concept to design a high Q microcavity. Utilizing the centrosymmetric characters of outer and inner microcavity, an ultra-high Q factor can be achieved without breaking the original mode characteristics. This device can also be used as multi band-stop filter in plasmonic system, which may have applications in integrated optical circuits.

Acknowledgments: This work is supported by the National Natural Science Foundation of China (60907003, 61671455); the Foundation of NUDT (JC13-02-13), the Hunan Provincial Natural Science Foundation of China (13JJ3001), and the Program for New Century Excellent Talents in University (NCET-12-0142).

Author Contributions: Zhaojian Zhang designed the simulations and wrote the paper; Junbo Yang disscussed and revised the paper; Dingbo Chen, Jingjing Zhang, Jie Huang, Xin He and Yunxin Han give some advises.

Conflicts of Interest: The authors declare no conflict of interest.

References

1. Ebbesen, Thomas W, A. Dereux, and C. W. Barnes. Surface plasmon subwavelength optics. *Nature* **2003**, *424.6950*, 824-830.

2. Wu, W. Ultra-high resolution filter and optical field modulator based on a surface plasmon polariton. *Optics Letters* **2016**, *41.10*, 2310.

298   3.   Wu, D. Numerical study of an ultra-broadband near-perfect solar absorber in the visible and near-infrared
299   region. *Optics Letters* **2017**, *42.3*, 450.
300   4.   Yu, Y., Si J, Ning Y. Plasmonic wavelength splitter based on a metal-insulator-metal waveguide with a
301   graded grating coupler. *Optics Letters* **2017**, *42.2*, 187.
302   5.   Chen, L. Numerical analysis of a near-infrared plasmonic refractive index sensor with high figure of merit
303   based on a fillet cavity. *Optics Express* **2016**, *24.9*, 9975.
304   6.   Tong, L. Recent advances in plasmonic sensors. *Sensors* **2014**, *14.5*, 7959.
305   7.   Y. Shen, J. H. Zhou, T. R. Liu, Y. T. Tao, R. B. Jiang, M. X. Liu, G. Xiao, J. Zhu, Z. K. Zhou, X. Wang, C. Jin,
306   and J. Wang, Plasmonic gold mushroom arrays with refractive index sensing figures of merit approaching
307   the theoretical limit. *Nat. Commun* **2013**, *4*, 2381.
308   8.   Srivastava, Triranjita, R. Das, and R. Jha. Highly Sensitive Plasmonic Temperature Sensor Based on
309   Photonic Crystal Surface Plasmon Waveguide. *Plasmonics* **2013**, *8.2*, 515-521.
310   9.   Maisonneuve, M. Phase sensitive sensor on plasmonic nanograting structures. *Optics Express* **2011**, *19.27*,
311   26318-24.
312   10. Elsayed, Mohamed Y., Y. Ismail, and M. A. Swillam. Semiconductor plasmonic gas sensor using on-chip
313   infrared spectroscopy. *Applied Physics* **2017**, *A 123*.1, 113.
314   11. Maier, Stefan A. Plasmonics: Fundamentals and Applications. *Springer Berlin* **2014**, *52.11*, 49-74.
315   12. Shu, Changgan. The sensing characteristics of plasmonic waveguide with a ring resonator. *Optics Express*
316   **2014**, *22.7*, 7669-77.
317   13. Yan, Shu Bin. A Refractive Index Sensor Based on a Metal-Insulator-Metal Waveguide-Coupled Ring
318   Resonator. *Sensors* **2015**, *15.11*, 29183-91.
319   14. Huang, Ye Xiong. A plasmonic refractive index sensor based on a MIM waveguide with a side-coupled
320   nanodisk resonator. *IEEE, International Conference on Embedded and Real-Time Computing Systems and
321   Applications IEEE* **2014**, 1-5.
322   15. Wu, Tiesheng. A nanometeric temperature sensor based on plasmonic waveguide with an ethanol-sealed
323   rectangular cavity. *Optics Communications* **2015**, *339*, 1-6.
324   16. Tang, Y. Refractive Index Sensor Based on Fano Resonances in Metal-Insulator-Metal Waveguides Coupled
325   with Resonators. *Sensors* **2017**, *17.4*, 784.
326   17. Zhang, Zhidong. Fano Resonance Based on Metal-Insulator-Metal Waveguide-Coupled Double
327   Rectangular Cavities for Plasmonic Nanosensors. *Sensors* **2016**, *16.5*, 642.
328   18. Zafar, Rukhsar, and M. Salim. Enhanced Figure of Merit in Fano Resonance-Based Plasmonic Refractive
329   Index Sensor. *IEEE Sensors Journal* **2015**, *15.11*, 6313-6317.
330   19. Zhao, X., Z. Zhang, and S. Yan. Tunable Fano Resonance in Asymmetric MIM Waveguide Structure. *Sensors*
331   **2017**, *17*, 7.
332   20. Chen, Jianjun. Coupled-Resonator-Induced Fano Resonances for Plasmonic Sensing with Ultra-High
333   Figure of Merits. *Plasmonics* **2013**, *8.4*, 1627-1631.
334   21. Hardy, Amos, and W. Streifer. Coupled mode theory of parallel waveguides. *Journal of Lightwave Technology*
335   **1985**, *3.5*, 1135-1146.
336   22. Marom, E, O. G. Ramer, and S. Ruschin. Relation between normal-mode and coupled-mode analyses of
337   parallel waveguides. *Quantum Electronics IEEE Journal* **1984**, 1311-1319.
338   23. Ameling, Ralf. Cavity-enhanced localized plasmon resonance sensing. *Applied Physics Letters* **2010**, *97.25*,
339   253116-253116-3.
340   24. Khurgin, J. B. How to face the loss in plasmonics and metamaterials. *Nature Nanotechnology* **2014**, 10(1), 2-
341   6.
342   25. Veronis, G., & Fan, S. Modes of subwavelength plasmonic slot waveguides. *Journal of Lightwave Technology*
343   *2007*, *25*(9), 2511-2521.
344   26. Naghizadeh, Solmaz, and S. E. Kocabas. Guidelines for designing 2D and 3D plasmonic stub resonators.
345   *Journal of the Optical Society of America B* **2017**, 34.1.
346   27. Limonov, M. F., Rybin, M. V., Poddubny, A. N., & Kivshar, Y. S. Fano resonances in photonics. *Nature
347   Photonics* **2017**, *11*(9), 543-554.
348   28. Elhadj, S., Singh, G., & Saraf, R. F. Optical properties of an immobilized dna monolayer from 255 to 700
349   nm. *Langmuir the Acs Journal of Surfaces & Colloids* **2004**, *20*(13), 5539.
350   29. Emiliyanov, G., Jensen, J. B., Bang, O., Hoiby, P. E., Pedersen, L. H., & Kjaer, E. M., et al.. Localized
351   biosensing with topas microstructured polymer optical fiber. *Optics Letters* **2007**, *32*(5), 460-462.

352 30. Ott, J. R., Heuck, M., Agger, C., Rasmussen, P. D., & Bang, O. Label-free and selective nonlinear fiber-optical
353   biosensing. *Optics Express* **2008**, *16*(25), 20834-47.
354 31. Markos, C., Town, G. E., Vlachos, K., Bang, O., & Yuan, W. Label-free biosensing with high sensitivity in
355   dual-core microstructured polymer optical fibers. *Optics Express* **2011**, *19*(8), 7790-8.
356 32. Rindorf, L., Jensen, J. B., Dufva, M., Pedersen, L. H., H?Iby, P. E., & Bang, O. Photonic crystal fiber long-
357   period gratings for biochemical sensing. *Optics Express* **2006**, *14*(18), 8224-31.
358 33. Georgios, & TSIGARIDAS. (2017). A study on refractive index sensors based on optical micro-ring
359   resonators. *Photonic sensors* **2017**, *7*(3), 217-225.
360 34. Gierak, J., Madouri, A., Biance, A. L., Bourhis, E., Patriarche, G., & Ulysse, C., et al. Sub-5nm fib direct
361   patterning of nanodevices. *Microelectronic Engineering* **2007**, *84*(5), 779-783.